The state of CO and CO_2 ices in the Kuiper Belt as seen by JWST

Brown, Michael E.; Fraser, Wesley C.

Publisher's version / Version de l'éditeur:
https://doi.org/10.3847/PSJ/ace2ba
The Planetary Science Journal, 4, 7, pp. 1-6, 2023-07-27

The Planetary Science Journal, 4:130 (6pp), 2023 July https://doi.org/10.3847/PSJ/ace2ba

The State of CO and CO_2 Ices in the Kuiper Belt as Seen by JWST

Michael E. Brown[1] and Wesley C. Fraser[2,3]
[1] Division of Geological and Planetary Sciences, California Institute of Technology, Pasadena, CA 91125, USA; mbrown@caltech.edu
[2] Herzberg Astronomy and Astrophysics Research Centre, National Research Council, 5071 W. Saanich Road, Victoria, BC V9E 2E7, Canada
[3] Department of Physics and Astronomy, University of Victoria, Elliott Building, 3800 Finnerty Road, Victoria, BC V8P 5C2, Canada
Received 2023 March 20; revised 2023 June 9; accepted 2023 June 21; published 2023 July 27

Abstract

JWST has shown that CO_2 and CO are common on the surfaces of objects in the Kuiper Belt and have apparent surface coverages even higher than that of water ice, though water ice is expected to be significantly more abundant in the bulk composition. Using full Mie scattering theory, we show that the high abundance and the unusual spectral behavior around the 4.26 μm ν_1 band of CO_2 can be explained by a surface covered in a few micron thick layer of ~1–2 μm CO_2 particles. CO is unstable at the temperatures in the Kuiper Belt, so the CO must be trapped in some more stable species. While hydrate clathrates or amorphous water ice are often invoked as a trapping mechanism for outer solar system ices, the expected spectral shift of the absorption line for a CO hydrate clathrates or trapping in amorphous ice is not seen, nor does the H_2O abundance appear to be high enough to explain the depth of the CO absorption line. Instead, we suggest that the CO is created via irradiation of CO_2 and trapped in the CO_2 grains during this process. The presence of a thin surface layer of CO_2 with embedded CO suggests volatile differentiation driving CO_2 from the interior as a major process driving the surface appearance of these mid-sized Kuiper Belt objects, but the mechanisms that control the small grain size and depth of the surface layer remain unclear.

Unified Astronomy Thesaurus concepts: Kuiper belt (893); Infrared spectroscopy (2285); Ice composition (2272)

1. Introduction

Observations from JWST have shown that CO_2 and CO ices are ubiquitous on the surfaces of small bodies in the outer solar system. (Hénault et al. 2023). CO and CO_2 are the most abundant volatiles in comets after H_2O, at a ~10% mixing ratio, and, presumably, major components of icy bodies in the outer solar system (Bockelée-Morvan & Biver 2017), but the difficulty of observing these species in their solid form means that little has been known of their distribution and abundance in the small body population today.

At the surface temperatures of the Kuiper Belt and even throughout some of the Centaur range, CO_2 should be stable, thus its presence in the outer solar system should come as little surprise. With its lower abundance than H_2O in comets, it should be expected to be a minor surface component on bodies wherever H_2O is exposed at the surface. CO, in contrast, is unstable to sublimation anywhere inside ~200 au, and thus would not be expected to appear on any small bodies in the Kuiper Belt (Sekanina 1992).

Here we use JWST spectra in the 0.8–5.2 μm range to examine the state and abundance of CO_2 and of CO on objects in the Kuiper Belt. We show that, contrary to expectation, CO_2 appears significantly more abundant on the surface of Kuiper Belt objects (KBOs) than does water ice and that CO is retained at temperatures significantly higher than its sublimation temperature. We find that both of these properties can be explained as a consequence of a thin layer of fine-grained CO_2 frost on these objects.

2. Observations and Data Reduction

A large selection of KBOs and Centaurs is being observed by JWST program 2418. An overview of the observations and first results is presented in N. Pinilla-Alonso et al. (2023, private communication). CO_2 and CO appear in many of the spectra, and the spectral appearance of the CO_2 can be roughly sorted by the shape of the spectrum near the 4.26 μm ν_3 absorption feature (Hénault et al. 2023). We examine two spectra, representative of the range of appearance of the CO_2 feature, in detail to try to understand the state and abundance of CO_2 and CO on these objects. Table 1 lists the two objects and their known characteristics, including diameter and albedo from Vilenius et al. (2012) and Fornasier et al. (2013) and orbital elements from JPL Horizons.[4]

Each object is observed using the NIRSPEC integral field unit (IFU) mode with the prism disperser (Böker et al. 2022; Jakobsen et al. 2022), giving a spectral resolution of $R \sim 30$–300 from 0.6 to 5.2 μm and a spatial scale of 0.″1 square within a 3″ square box. Each of the KBOs appears as a point source. We have experimented with multiple methods for spectral extraction, and we find that a modification of the standard JWST pipeline (version #1.8.5; Bushouse et al. 2022)[5] currently gives the best results. We begin our data analysis with the Level 2 "rate" files, which are the calibrated two-dimensional detector images showing individual spectra from all 30 of the IFU slits. Examination of these files readily shows the effects of $1/f$ signal modulation caused by electronic drifts during the detector readout. Many of the detector pixels are not exposed to the sky and so can be used to measure and remove this modulation. We use the Level 2 "cal" files to find unilluminated pixels, and, for each pixel in the "rate" image,

[4] ssd.jpl.nasa.gov
[5] Using the JWST Calibration Reference Data System (CRDS; https://jwst-crds.stsci.edu) context file `jwst_1027.pmap`.

Table 1
Properties of the Observed KBOs

Name	2005 RN43	2002 TC302
Diameter (km)	679^{+55}_{-73}	584^{+106}_{-88}
Absolute magnitude (H)	3.89 ± 0.05	4.17 ± 0.1
Albedo	$0.11^{+.03}_{-.02}$	$0.11^{+0.05}_{-0.03}$
Semimajor axis (au)	41.8	55.7
Eccentricity	0.03	0.30
Inclination (deg)	19.2	35.0
Date of observation	2022 Nov 3	2023 Jan 2
Heliocentric distance (au)	40.6	42.9

we take the median of all unilluminated pixels in a column within $\pm$150 rows to define the modulation and subtract it from the "rate" image. The standard pipeline is then run on the new "rate" file, including the AssignWcs, MSAFlagOpen, SourceType, FlatField, PathLoss, and Photom steps. The final step in the standard pipeline is the CubeBuild, which converts the two-dimensional spectral images into three-dimensional spectral cubes. We circumvent as much of the interpolation required for mapping the slits to on-sky positions by forcing the pipeline to build the cubes with one axis parallel to the slits and one perpendicular to the slits (using the "internal_cal" geometry in CubeBuild). A single column of these cubes corresponds to a single slit.

Significant background appears in the nontarget parts of the spectral cubes, particularly at the shortest and longest wavelengths. We remove this background by taking the median of all of the pixels at each wavelength that are 5 pixels or more distant from the center of the target. Dithered images could be used for background subtraction, but the dither positions are often too closely spaced to use effectively. Significant numbers of bad pixels appear in the image cubes, suggesting that point-spread function (PSF) fitting with robust outlier rejection could be a profitable method of spectral extraction. Unfortunately, fitting using calculated PSFs (from, i.e., WebbPSF[6]) suffers from the undersampling of the PSF by the detector, even with these minimally resampled cubes. In these data, the undersampling of the PSF causes spectral ripples in individual pixels of the image cube. The ripples are caused as the peak of the PSF slowly moves from the center of the pixel to the edge and then to an adjacent pixel as a function of wavelength. The frequency of these ripples thus corresponds to the frequency of the spectral trace moving from pixel to pixel, which occurs once every $\sim$200 spectral pixels. The PSF, as sampled by the detector, thus also changes over this pixel scale in a manner not currently captured by any of the available PSF modeling tools. We circumvent this difficulty by constructing an empirical PSF at each wavelength from the median of the spectral images within 25 pixels of that wavelength normalized to a total value of unity. We then divide the spectral image by the empirical PSF at that wavelength and take the median of this division within a 3 pixel radius as the brightness at that pixel. The final spectrum is thus free of the pixel-to-pixel ripples introduced by the PSF undersampling.

To obtain the relative reflectance of the object, we divide the extracted spectrum by an identically reduced spectrum of a PRISM observation of the solar analog 2MASS J16194609+5534178 (Gordon et al. 2022) from Program # 1128. This division removes any wavelength-dependent calibration issues in the JWST pipeline, corrects for the wavelength-dependent PSF changes, and converts the flux to a relative reflectance. We normalize each spectrum to have a median value of unity between 1.5 and 2.5 μm. The final spectra of our two example objects are shown in Figure 1.

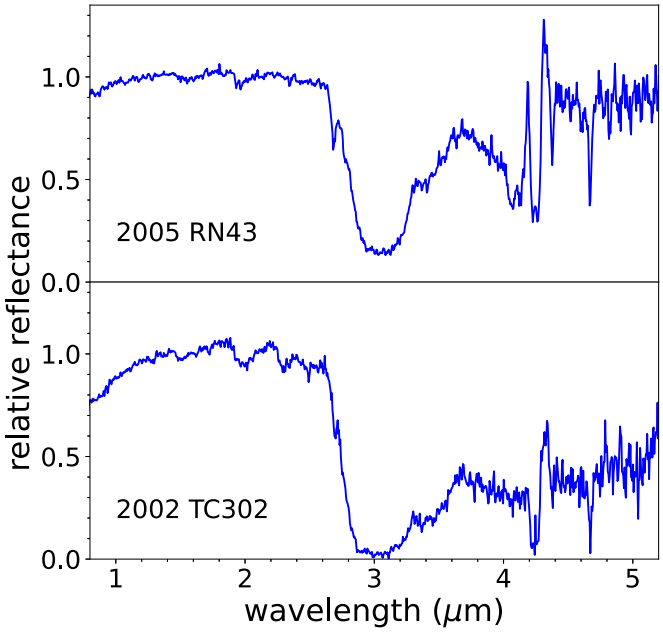

Figure 1. The spectra of two representative KBOs from the sample. Each shows subtle 1.5 and 2.0 μ absorption features indicative of a modest exposure of water ice, deep 3 μm absorption consistent with a tholin-like processed organic surface, a broad 3.4–3.6 μm absorption owing to organic materials, a narrow 4.6 μm absorption from CO, and numerous and variable features from 4.0 to 4.4 μm all attributable to CO_2.

3. Results and Modeling

The features surrounding the deep 4.26 μm CO_2 absorption on 2005 RN43 and 2002 TC302 are unlike any reflectance spectrum previously seen. A 4.26 μm absorption has been seen on the icy satellites of Jupiter (Hibbitts et al. 2003) and Saturn (Cruikshank et al. 2010), but in all cases the absorption is modest and shows no additional absorptions nearby. In these cases, however, CO_2 is not in pure form but must be trapped as a minor constituent in a background material to allow the CO_2 to be stable at the elevated temperatures of these satellites. These new KBO observations are the first at temperatures where pure CO_2 is stable and potentially dominating the spectral region around the 4.26 μm line. We thus carefully examine the reflectivity of pure CO_2 through this region.

Between 4.0 and 4.5 μm, CO_2 has not just a large change in absorptivity, but its real index of refraction goes from its typical value of $\sim$1.3 at shorter wavelengths, approaches 0 near 4.19 μm, climbs above a value of 5 at 4.27 μm, and then drops to 1.5 at longer wavelengths (Gerakines & Hudson 2020). Dramatic changes such as these in the real index of refraction alongside large changes in the imaginary index of refraction (related to absorption) cause complicated spectral behavior. In Figure 2 we plot the spectrum of both objects, along with the real and imaginary indices of refraction. As can be seen, the most anomalous-appearing spectral behavior of 2005 RN43 appears at precisely the locations where the real index of

[6] https://www.stsci.edu/jwst/science-planning/proposal-planning-toolbox/psf-simulation-tool

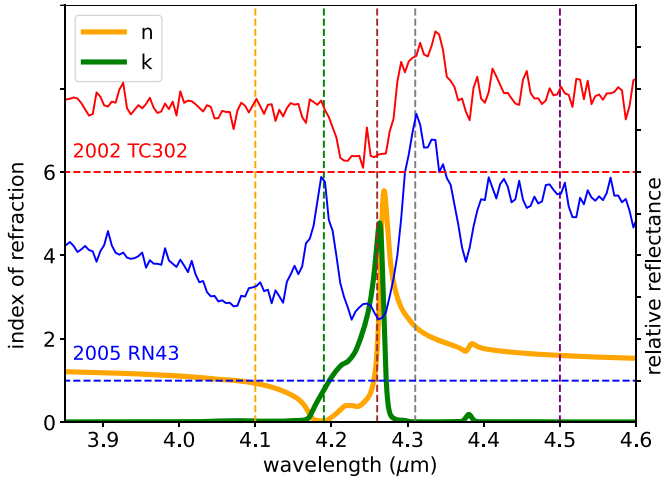

Figure 2. The real (n) and imaginary (k) indices of refraction of CO_2 compared to the spectra of 2005 RN43 and 2002 TC302, which are both offset for clarity with their zero-points (shown as blue and red horizontal dashed lines, respectively). Major spectral features on both objects occur at the locations marked by dashed lines, including when the real index passes through unity, when it approaches zero, where the imaginary index peaks, and where the imaginary index returns to near zero while the real index changes rapidly.

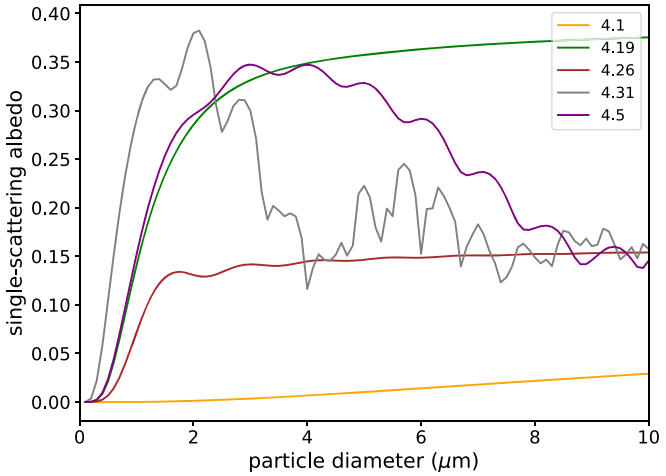

Figure 3. The geometric albedo from a collection of Mie scattering particles from 0.1 to 10 μm in diameter. The colors of the lines correspond to the scattering behavior at the different wavelengths of the same colors of the dashed lines in Figure 2. The strong changes in both the real and imaginary index of refraction across this spectral region make the spectral behavior an extremely complicated and sensitive function of particle size.

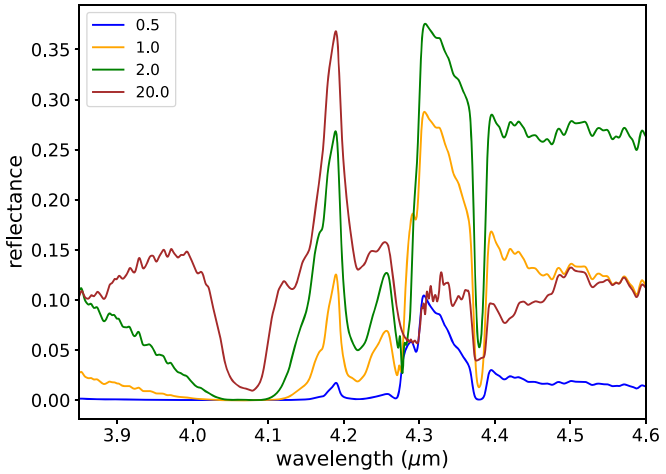

Figure 4. Full spectral models of a collection of Mie scattering CO_2 particles of four particle sizes. The prominent peaks at both 4.19 and 4.34 μm are only seen for particle diameters of 1–2 μm.

refraction goes through unity, where it approaches zero, where the imaginary index peaks, and where the imaginary index falls back to zero but the real index changes rapidly.

Because of the complexity of the behavior in this region, we resort to full Mie theory to understand the reflectivity across this wavelength region. We use the Python package *miepython* (Prahl 2023), which implements and has been validated against the Wiscombe (1979) algorithm, to calculate the single-scattering albedo of spherical CO_2 particles from very small 0.1 μm particles, in the Rayleigh scattering regime, to 100 μm particles, in the geometric optics regime. Using the single-scattering albedo, we calculate the geometric albedo assuming a uniform surface of isotropic scatters using the formulation of Hapke (1993), Equation (10.37).

Mie scattering calculations are only strictly accurate for well-separated spheres, which is clearly not the case on a planetary surface. Mustard & Hays (1997) investigated the spectra of olivine and quartz powders with grain sizes near and below the wavelength of spectral features and found that a combined Mie theory/Hapke modeling approach as used above provides the best modeling match to laboratory data. Some limitations to this approach are discussed below.

Figure 3 shows the geometric albedo as a function of the particle size of the scatterers for the five key wavelengths shown in Figure 2. One point is immediately apparent from this figure. For the geometric albedo at 4.31 μm to rise above that at the 4.19 μm peak or at the 4.5 μm continuum beyond that, the grains must be smaller than about 2 μm. It is also clear that as particles approach the Rayleigh scattering regime, the contrast between the peak at 4.19 μm and the trough at 4.26 μm becomes increasingly smaller, while the overall albedo declines quickly. To understand the full spectrum through this region we show, in Figure 4, model spectra of a uniform isotropic surface of Mie scattering particles of various sizes. For 0.5 μm particles, the 4.26 μm absorption no longer appears distinct, while at sizes of 1–2 μm, the doublet in that absorption band—which is clear in the data—emerges. We conclude that the main structures seen in the spectrum of 2005 RN43 around 4.26 μm, namely the absorption near 4.10 μm, the narrow peak at 4.19 μm, the doublet absorption around 4.26 μm, and the broader strong peak at 4.31 μm can all be explained if this object is covered in CO_2 grains between about 1 and 2 μm in diameter. The behavior seen in 2002 TC302, with a single peak redward of the deep CO_2 absorption, is not seen in these models.

One feature prevalent in all of the model spectra with small CO_2 grains is that the albedo is a minimum near 4.1 μm, where the real index of refraction passes through unity. The imaginary index of refraction is small but nonzero at this wavelength, so light will pass through all grains unaffected by refraction or reflection, and simply be absorbed after passage through a large number of grains. The albedo will thus stay near zero. In the real spectra of the KBOs observed in the full program, however, the albedo is always lowest in the 4.23/4.26 μm absorption doublet (Hénault et al. 2023). Such a spectral shape can be a simple consequence of reflection from a layer of CO_2 particles covering a reflective medium. At 4.1 μm the CO_2 is essentially transparent, so it will propagate through the CO_2

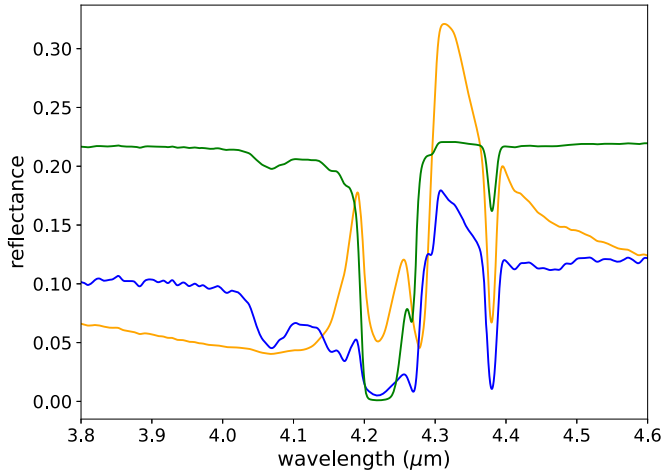

Figure 5. Spectral models of a thin layer of CO_2 particles overlying a reflective medium. Models such as these are needed to correctly reproduce the nonzero albedo at 4.1 μm where CO_2 becomes essentially transparent. Slight changes in grain sizes and CO_2 layer thickness give rise to many different apparent spectral types, allowing the full range of CO_2 detected in the Kuiper Belt to be explained. The three models shown have background albedo, CO_2 grain diameter, and CO_2 layer thickness of 0.05, 2, and 2 μm (orange); 0.16, 0.7, and 10 μm (blue); and 0.23, 0.5, and 1 μm (green).

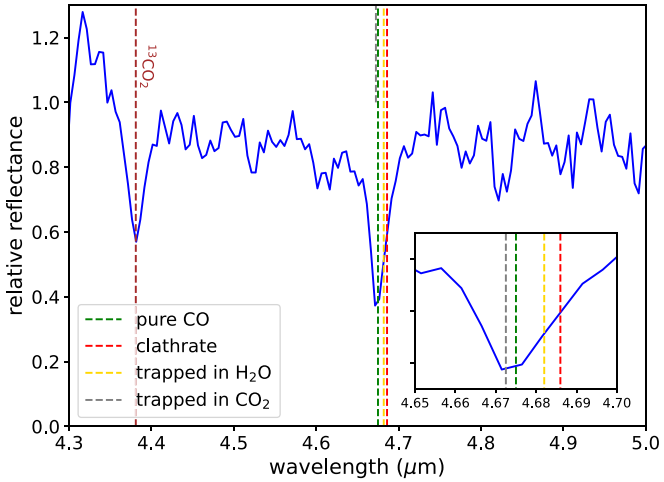

Figure 6. A small portion of the spectrum of 2005 RN43 showing both the $^{13}CO_2$ line, which we use as a wavelength reference, and the CO line. The wavelength of the CO does not match that of CO clathrate hydrates or CO trapped in amorphous ice, but is a close match to pure CO (which is unstable at this temperature), and also to CO trapped in CO_2 ice.

layer and reflect off of the underlying surface. At 4.23/4.26 μm the light can—depending on the optical depth of the layer—still be fully absorbed within the CO_2 layer, leading to deeper absorption lines. We model this behavior using the formalism for layered media of Hapke (1993; Equation 9.14). We assume a thin layer of CO_2 particles with a depth of l and particle diameter of d overlying a surface with a constant geometric albedo of a. Figure 5 shows three spectral models with only small changes in these parameters. These models reproduce the basic behavior of both the 2005 RN43-type of CO_2 spectrum, with sharp lines on either side of the main absorption, and the 2002 TC302-type spectrum, with a single line redward of the CO_2 absorption. In the models shown here, the CO_2 layer is between 1 (orange and green lines) and 6 (blue line) particle diameters thick.

The contrast between the continuum and the peaks seen in these modeled spectra is higher than that seen in the real KBOs. Interestingly, the same behavior is seen by Mustard & Hays (1997) in the laboratory versus modeled spectra of quartz, which has similar values of both the real and imaginary index of refraction in the 9 μm region as CO_2 does in the 4.3 μm region. We thus suspect that the too-high contrast of the models is a consequence of the difficulties of using Mie theory to model tight-packed grains such as these and that we are indeed observing a surface covered with such small grains.

An interesting consequence of the highly variable nature of the spectra from 4.0 to 4.4 μm is the difficulty of quantitatively interpreting the $^{13}CO_2$ line at 4.38 μm. In Figure 5, for example, the $^{13}CO_2$ abundance is just the terrestrial value and is seen in the measured values of n and k simply because of the natural contamination of the laboratory sample of CO_2. In each modeled spectrum, however, though the $^{12}C/^{13}C$ ratio is identical, the depth of the $^{13}CO_2$ line is variable. The variability of this line in these models highlights the difficulty of using these observations to make precise quantitative statements about the $^{12}C/^{13}C$ ratio in these objects. Nonetheless, the observations of the $^{13}CO_2$ line on these objects do not appear strongly inconsistent with the strength seen in the spectral models, suggesting that the isotopic ratio is not strongly inconsistent with the terrestrial value of 89. Such a finding is not surprising given the measurements of the $^{12}C/^{13}C$ in cometary C_2, CN, and HCN, which also give values close to the terrestrial value (Bockelée-Morvan et al. 2015).

4. CO

The presence of CO on small bodies in the Kuiper Belt requires that the CO be trapped to prevent sublimation at these temperatures. Trapping of CO in amorphous water ice or as a clathrate hydrate is often invoked as a possible process important in the outer solar system (Bar-Nun et al. 1985; Gautier & Hersant 2005). The ν_1 absorption feature of enclathrated CO is spectrally shifted from its position at 4.675 μm in pure CO ice (Dartois 2011). In Figure 6, we show a detail of the spectrum of 2005 RN43 near the CO region.

Measuring the precise wavelength of the CO feature is complicated by the uncertainty that still remains in the wavelength scale of the PRISM mode observations. To understand possible wavelength uncertainties, we examined wavelengths of known emission lines in a star-forming region of NGC 7319 (Program 2732). After correcting for the redshift, we find that beyond 4 μm, the wavelength scale is off by about half a pixel (~0.003 μm) and that the wavelength scale between 4 and 5 μm likewise changes by about half a pixel. To account for this effect as best as possible, we set the wavelength scale by forcing the $^{13}CO_2$ absorption to occur precisely at 4.381 μm (which involves a 0.005 μm shift from the nominal wavelength solution). While trapped CO_2 will have a wavelength shift from this nominal wavelength (for example on Ganymede; Hibbitts et al. 2003), the high abundance of CO_2 ensures that we are not seeing a small trapped population here. Thus, based on the analysis of NGC 7319, the wavelength solution at the location of the CO line should be accurate to within at least a 0.005 μm pixel.

With this wavelength solution, the CO line on 2005 RN43 appears at the 4.675 μm wavelength of pure CO and not at the 4.686 μm wavelength of CO clathrate nor the 4.682 μm wavelength measured for the trapping of amorphous water

ice at 50 K (Sandford & Allamandola 1988). This 0.007–0.011 μm difference is well above any expected wavelength uncertainty. The lack of evidence for a water ice CO clathrate or trapping in amorphous water ice is perhaps not surprising given the weak 1.5 and 2.0 μm absorption lines of water ice.

Given the large surface coverage of CO_2 on these objects, we consider CO trapped in this species. Simon et al. (2019) examined the trapping of CO in CO_2 and found that such trapping can be even more efficient than trapping in H_2O. The trapped CO was stable at temperatures as high as 80 K, even higher than the expected surface temperatures of these objects. At 50 K, the wavelength of the absorption from the trapped CO is 4.673 μm, consistent with the position of the line seen here. While the wavelength match is good, the mechanism of gas trapping used in these experiments—the mechanical mixing of the gasses before freezing onto a substrate at 17 K—does not obviously apply to these objects.

A more promising CO-trapping mechanism involves both the production and trapping of CO in CO_2 through irradiation. Martín-Doménech et al. (2015) showed the UV irradiation of CO_2 creates CO, which remains stable even at temperatures as high as 90 K. The trapping mechanism here is different from either the enclathration or the physical trapping discussed above, so it is possible that the wavelength shift of CO trapped in this manner is different from those mechanisms. Unfortunately, the wavelength of the CO absorption at temperatures relevant to the Kuiper Belt was not measured. Physically and chemically, this explanation for the presence of CO at elevated temperatures seems most promising, but laboratory measurement of the wavelength of CO created and trapped at KBO-like temperatures is clearly needed.

5. Discussion

The presence of a thin layer of fine-grained CO_2 appears common on objects in the Kuiper Belt. CO is likewise common and must be trapped within some thermally stable material. These two observations lead to a natural model for the presence of both of these molecules. We posit that CO_2 from the interior of these objects is heated and diffuses toward the surface where it is retained as a fine-grained frost. Irradiation of the CO_2 (UV, solar wind, and/or cosmic ray) then produces CO within these CO_2 grains.

This simple idea hides some difficult complexities. Many of the other KBOs in this program are seen to have CO_2 features manifesting like the two discussed here (Hénault et al. 2023). Given the high level of sensitivity of the spectral models to the grain size and layer thickness, the lack of a wider variety of spectral types is surprising. Hapke (1993) argues that for grain sizes much smaller than the wavelength of the light, the scattered radiance tends to sample inhomogeneities in the medium that are of order of the wavelength divided by pi, which is 1.35 μm in our case and remarkably close to the preferred range of particle size solutions that we find. In this case, the observations would be indicative of grains of a few microns or smaller without the need to be a specific size, at least partially alleviating the fine-tuning problem.

The thickness of the CO_2 layer also exerts a strong control on the modeled spectrum, in particular in the albedo at 4.1 μm, where $n = 1$ and CO_2 is transparent. Layers larger than a few microns begin to look more like the pure CO_2 spectra of Figure 4 and are hard to reconcile with the observations. The need to use thin layers in the models is no obvious consequence of deficiencies of the Mie or Hapke theory, so we believe that such thin layers are indeed intrinsic to the KBOs. How such thin layers are formed and preserved with such a small thickness range is unclear, but the tight constraints suggest an ongoing balance between formation and destruction that must be common to these objects.

This process of outward volatile transport should operate most strongly on the larger KBOs, which have received the most heating. The size range probed in this program is modest, so smaller objects will have to be observed to see if this prediction is borne out. No modeling of interior volatile evolution on objects of these sizes has yet been attempted, though, for smaller sizes, CO_2 is thought to remain unchanged by the smaller amount of interior heating (De Sanctis et al. 2001). Understanding the implications of this new body of data will be a critical next step in piecing together the chemical history of the outer solar system.

Acknowledgments

We would like to thank John Stansberry and two anonymous reviewers for interesting comments on the manuscript. This work is based on observations made with the NASA/ESA/CSA James Webb Space Telescope. The data were obtained from the Mikulski Archive for Space Telescopes at the Space Telescope Science Institute, which is operated by the Association of Universities for Research in Astronomy, Inc., under NASA contract NAS 5-03127 for JWST. These observations are associated with program # 2418 and the specific observations analyzed can be accessed via doi:10.17909/tnkm-hq35 (Brown 2023). The authors acknowledge the team led by PI N. Pinilla-Alonso for developing their observing program with a zero-exclusive-access period.

Facility: JWST (NIRSPEC).

Software: JWST pipeline (version #1.8.5; Bushouse et al. 2022), miepython (Prahl 2023).[7]

ORCID iDs

Michael E. Brown https://orcid.org/0000-0002-8255-0545
Wesley C. Fraser https://orcid.org/0000-0001-6680-6558

References

Bar-Nun, A., Herman, G., Laufer, D., & Rappaport, M. L. 1985, Icar, 63, 317
Bockelée-Morvan, D., & Biver, N. 2017, RSPTA, 375, 20160252
Bockelée-Morvan, D., Calmonte, U., Charnley, S., et al. 2015, SSRv, 197, 47
Böker, T., Arribas, S., Lützgendorf, N., et al. 2022, A&A, 661, A82
Brown, M. 2023, Spectra of 2005 RN43 and 2002 TC302, MAST, doi:10.17909/tnkm-hq35
Bushouse, H., Eisenhamer, J., Dencheva, N., et al. 2022, JWST Calibration Pipeline, v1.8.5, Zenodo, doi:10.5281/zenodo.7429939
Cruikshank, D. P., Meyer, A. W., Brown, R. H., et al. 2010, Icar, 206, 561
Dartois, E. 2011, Icar, 212, 950
De Sanctis, M. C., Capria, M. T., & Coradini, A. 2001, AJ, 121, 2792
Fornasier, S., Lellouch, E., Müller, T., et al. 2013, A&A, 555, A15
Gautier, D., & Hersant, F. 2005, SSRv, 116, 25
Gerakines, P. A., & Hudson, R. L. 2020, ApJ, 901, 52
Gordon, K. D., Bohlin, R., Sloan, G. C., et al. 2022, AJ, 163, 267
Hapke, B. 1993, Theory of Reflectance and Emittance Spectroscopy (Cambridge: Cambridge Univ. Press)
Hénault, E., Pinilla-Alonson, N., Holler, B., et al. 2023, ResearchSquare, doi:10.21203/rs.3.rs-2887978/v1

[7] http://miepython.readthedocs.io

Hibbitts, C. A., Pappalardo, R. T., Hansen, G. B., & McCord, T. B. 2003, JGRE, 108, 5036
Jakobsen, P., Ferruit, P., Alves de Oliveira, C., et al. 2022, A&A, 661, A80
Martín-Doménech, R., Manzano-Santamaría, J., Muñoz Caro, G. M., et al. 2015, A&A, 584, A14
Mustard, J. F., & Hays, J. E. 1997, Icar, 125, 145
Prahl, S. 2023, miepython, v2.3.2, Zenodo, doi:10.5281/zenodo.7949403
Sandford, S. A., & Allamandola, L. J. 1988, Icar, 76, 201
Sekanina, Z. 1992, in Asteroids, Comets, Meteors 1991, ed. A. W. Harris & E. Bowell (Houston, TX: Lunar and Planetary Society), 545
Simon, A., Öberg, K. I., Rajappan, M., & Maksiutenko, P. 2019, ApJ, 883, 21
Vilenius, E., Kiss, C., Mommert, M., et al. 2012, A&A, 541, A94
Wiscombe, W. J. 1979, Mie Scattering Calculations; Advances in Technique and Fast, Vector-speed Computer Codes PB-301388, NCAR, https://cir.nii.ac.jp/crid/1571135649197161856